Filtering After Shading With Stochastic Texture Filtering

MATT PHARR*, NVIDIA, USA
BARTLOMIEJ WRONSKI*, NVIDIA, USA
MARCO SALVI, NVIDIA, USA
MARCOS FAJARDO, Shiokara–Engawa Research, Spain

2D texture maps and 3D voxel arrays are widely used to add rich detail to the surfaces and volumes of rendered scenes, and filtered texture lookups are integral to producing high-quality imagery. We show that applying the texture filter after evaluating shading generally gives more accurate imagery than filtering textures before BSDF evaluation, as is current practice. These benefits are not merely theoretical, but are apparent in common cases. We demonstrate that practical and efficient filtering after shading is possible through the use of stochastic sampling of texture filters.

Stochastic texture filtering offers additional benefits, including efficient implementation of high-quality texture filters and efficient filtering of textures stored in compressed and sparse data structures, including neural representations. We demonstrate applications in both real-time and offline rendering and show that the additional error from stochastic filtering is minimal. We find that this error is handled well by either spatiotemporal denoising or moderate pixel sampling rates.

CCS Concepts: • **Computing methodologies → Texturing**; *Antialiasing*; Ray tracing; Rasterization.

ACM Reference Format:
Matt Pharr, Bartlomiej Wronski, Marco Salvi, and Marcos Fajardo. 2024. Filtering After Shading With Stochastic Texture Filtering. *Proc. ACM Comput. Graph. Interact. Tech.* 7, 1, Article 1 (May 2024), 29 pages. https://doi.org/10.1145/3651293

1 INTRODUCTION

Image texture maps play a crucial role in achieving rich surface detail in most rendered images. The availability of advanced texture painting tools provides artists with precise and natural control over the material appearance. Three-dimensional voxel grids play a similar role for volumetric effects like clouds, smoke, and fire, allowing detailed offline physical simulations to be used. The number and resolution of both has continued to increase over the years.

Typical practice in rendering is to perform filtered texture lookups to find the values of shading parameters. We demonstrate that filtering *before* shading introduces error if those parameters make a nonlinear contribution to the final result. We show that applying the texture filter *after* shading instead gives a more accurate result in these cases. However, a naive implementation of filtering after shading imposes an increased computational cost. A family of efficient *stochastic texture filtering* algorithms allows to efficiently filter after shading, potentially with only a single texel access for each texture map lookup (Figure 1).

*Equal contributions

Authors' addresses: Matt Pharr, NVIDIA, Santa Clara, California, USA; Bartlomiej Wronski, NVIDIA, Santa Clara, California, USA; Marco Salvi, NVIDIA, Santa Clara, California, USA; Marcos Fajardo, Shiokara–Engawa Research, Madrid, Spain.

ACM 2577-6193/2024/5-ART1
https://doi.org/10.1145/3651293

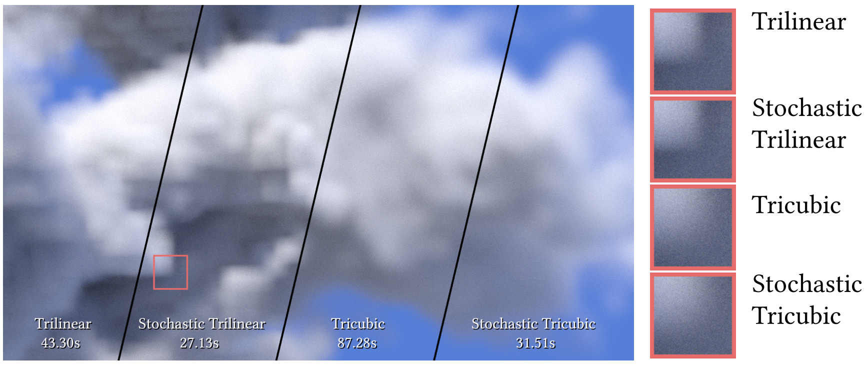

Fig. 1. A section of the *Disney Cloud* rendered with path tracing. Trilinear filtering leads to blocky artifacts in the image. Tricubic filtering gives a much better result, but requires 64 voxel lookups to compute each filtered value. Stochastic filtering performs a single voxel lookup yet provides indistinguishable results, with rendering time speedups of 1.60× and 2.77× for the trilinear and tricubic filters. Times reported are for *pbrt-v4* running on an NVIDIA 4090 RTX GPU, rendering at 1080p with 256 samples per pixel.

Stochastic texture filtering demonstrates other performance and filtering quality advantages. It is especially beneficial for textures stored using custom representations such as UDIM's adaptive tiling, multi-level sparse grids [Museth 2013], or neural representations [Vaidyanathan et al. 2023], which are generally incompatible with hardware-accelerated filtering and have computationally costly texture accesses.

We note that the idea of stochastic texture filtering has been presented earlier in the literature and used in production. However, we are not aware of a comprehensive or formal overview of its methods or analysis of their advantages and drawbacks. Our contributions are as follows:

- We show that using stochastic texture filtering allows filtering after shading, rather than filtering the texture data before shading. Doing so produces more accurate and appearance-preserving results, especially during minification.
- We describe two ways of stochastically filtering textures, discuss their theoretical and practical differences and connect them to prior work.
- We demonstrate that in real-time rendering the additional noise introduced by stochastic filtering is effectively suppressed by using spatiotemporal reconstruction algorithms and blue-noise sampling patterns. We further show that for offline rendering moderate pixel sampling rates are sufficient to handle the noise well.
- Finally, we show that stochastic texture filtering can further improve image quality by allowing the use of high-quality texture filters at a lower cost than trilinear filtering.

2 BACKGROUND AND PREVIOUS WORK

The use of image textures in rendering dates to Blinn and Newell [Blinn and Newell 1976; Catmull 1974]. See Heckbert's survey article [1986] for comprehensive coverage of early work in this area. Nehab and Hoppe [2011] present a modern take on the topic of texture interpolation and prefiltering and expand it to different prefilters.

Monte Carlo estimation via stochastic sampling [Kajiya 1986] has become the foundation of most approaches to rendering today. Production rendering has embraced path tracing for over a decade [Křivánek et al. 2010], and real-time rendering begins to adopt path tracing as well [Clarberg et al. 2022]. Although lighting integrals are evaluated stochastically, their integrands are usually evaluated analytically. Integrands that are themselves stochastic have been used for complex BSDF models [Guo et al. 2018; Heitz et al. 2016], multi-lobe BSDF evaluation [Szécsi et al. 2003] and for many light sampling [Estevez and Kulla 2018; Shirley et al. 1996].

Real-time rendering has also embraced stochastic approaches, including stochastic texturing. UV jittering and using nearest-neighbor filtering as an alternative to bilinear filtering dates as far back as the 1990s and the video game *Star Trek: 25th Anniversary* [Interplay 1992] and the original *Unreal Engine* [Sweeney and Nettle 2000]. More contemporary examples include stochastic alpha testing [Enderton et al. 2010; Wyman and McGuire 2017], filtering of reflections [Stachowiak 2015], and raytraced ambient occlusion [Barré-Brisebois et al. 2019]. Temporal anti-aliasing (TAA) [Karis 2014; Yang et al. 2020] and temporal super-resolution (TSS) [Liu 2022] are key enabling technologies for these approaches. Both are based on recursive filters and exponential-moving-averaging with adaptive history modification and rejection. *Negative MIP biasing* is often used with screen-space jittering for sharper images and approximate anisotropic filtering when TAA and TSS are used. We formalize this approach, analyze how it deviates from anisotropic filtering, and show why it produces a more accurate filtered shading result than standard texture filtering.

The motivation for our work includes the stochastic filtering algorithms introduced by Hofmann et al. [Hofmann et al. 2021] and Vaidyanathan et al. [Vaidyanathan et al. 2023], who used stochastic trilinear filtering to improve performance. They showed significant speedups by avoiding evaluating an expensive decompression algorithm multiple times per pixel. The *OpenImageIO* library [Gritz 2022] also supports stochastic sampling of MIP levels and anisotropic samples, and Lee et al. [Lee et al. 2017] replaced filtered texture lookups with nearest-neighbor point samples in the *MoonRay* renderer, relying on the high sampling rates common in film production to avoid texture aliasing. We expand on their results, analyze the effect of stochastic texture filtering, and show how to use a wider range of texture filters.

Applying filtering after a rendering non-linearity can be traced to the concept of pre-multiplied alpha [Porter and Duff 1984], where alpha pre-multiplication avoids nonsensical interpolated values during magnification and filtering of alpha-composited textures. The pioneering work of Reeves et al. [Reeves et al. 1987] on shadow map filtering was the first to explicitly distinguish between filtering before shading versus filtering afterward. Their percentage closer filtering algorithm is based on filtering binary visibility rather than depth. We discuss how this approach applies to other aspects of rendering and analyze the effects of swapping the filtering and shading order.

2.1 Texture Filtering

Textures are represented by discrete, uniformly-spaced samples $t_{u,v}$[1]. Following Heckbert [1989], they can be interpreted as a set of scaled and translated Dirac delta functions:

$$t(u,v) = \sum_{u'} \sum_{v'} \delta(u-u')\delta(v-v')\, t_{u',v'} \tag{1}$$

The texture function $t(u,v)$ is defined over $\mathbb{R}^2$ but is only non-zero at the texel locations. A continuous texture function can be defined by specifying a reconstruction filter f_r and convolving it with the texture function:

$$t_\mathrm{r}(u,v) = t \otimes f_\mathrm{r} = \iint t(u',v')\, f_\mathrm{r}(u-u', v-v')\, \mathrm{d}u'\, \mathrm{d}v', \tag{2}$$

where $t \otimes f_\mathrm{r}$ represents the convolution of t with f_r. Bilinear and bicubic filters are commonly used for the reconstruction filter.

[1]Without loss of generality, in this section, we assume the use of 2D textures.

The continuous texture function may contain higher frequency detail than can be captured by the pixel sampling Nyquist rate. Sampling such a signal would lead to visible aliasing in the final image. In order to eliminate aliasing, the continuous texture function may be convolved with a suitable low-pass filter f_l to remove high frequencies. The pixel-space Nyquist frequency defines the filter parameters, which can be found either by projecting a pixel's extent onto the surface tangent plane, by taking finite differences with adjacent pixels, or via ray differentials or a related technique [Akenine-Möller et al. 2021; Igehy 1999]. This gives the final filtered texture function:

$$t_\mathrm{f}(u,v) = t \otimes f_\mathrm{r} \otimes f_\mathrm{l}. \tag{3}$$

Because the original texture function $t(u,v)$ is only non-zero at discrete locations and because practical filters typically have finite extent, t_f takes the form of a sum over a limited number of texture samples. For notational simplicity, we will generally write it as a single sum.

Under magnification, the low-pass filter is not necessary, as the shading rate is higher than the discrete texture Nyquist rate. Similarly, under minification, neglecting the reconstruction filter f_r generally introduces little error. Alternatively, a single *unified texture filter* that handles both reconstruction and low-pass filtering may also be used. The elliptically weighted average (EWA) filter [Greene and Heckbert 1986; Heckbert 1989] is a notable example.

Filtering texture lookups is expensive since the low-pass filter f_l requires accessing multiple texture samples and may have different parameters at each sample. Prefiltering textures into multiple resolutions that are stored in image pyramids substantially reduces the number of texels accessed by the low-pass filter [Williams 1983]. Nehab and Hoppe [2011] expanded the concept of texture prefiltering to different prefilters and reconstruction filters. For both prefiltering and lowpass filtering, several techniques that approximate high-quality filters using multiple hardware-accelerated bilinear lookups have been developed [Barkans 1997; Cant and Shrubsole 2000; McCormack et al. 1999].

2.2 Sampling Techniques

We briefly summarize the common sampling techniques we use. See the books by Pharr et al. [2023] or Ross [2019] for further background. In the following, we will use ξ to denote uniform random variables in $[0,1)$ and angled brackets to denote expectation.

Separable functions: An n-dimensional function that is a product of 1D functions can be sampled by independently sampling each dimension. Many filters used for textures, including Gaussian and polynomials (linear, cubic, etc.) are separable.

Weighted sums: Since Equation 3 reduces to a weighted sum over texture samples, given weights w_i that sum to 1 and texture values t_i, the filtered texture value is given by

$$F = \sum_{i=1}^{n} w_i\, t_i. \tag{4}$$

If a term j of the sum is sampled with probability equal to w_i, then an unbiased estimate of F is given by the corresponding texture value, unweighted:

$$\langle F \rangle = t_j. \tag{5}$$

This is a special case of sampling a term according to probabilities $p_i \propto w_i$ and applying the standard Monte Carlo estimator f_j/p_j.

Uniform sample reuse: Whenever a 1D random variable ξ is used to make a discrete sampling decision based on a probability p, a new independent random variable $\xi' \in [0,1)$ can be derived from ξ [Shirley et al. 1996]:

$$\xi' = \begin{cases} \xi/p & \text{if } \xi < p \\ (\xi - p)/(1-p) & \text{otherwise.} \end{cases} \tag{6}$$

This technique can be useful when ξ is well-distributed (e.g., with a blue noise spectrum [Georgiev and Fajardo 2016] or with low discrepancy), allowing additional dimensions to benefit from ξ's distribution as well as saving the cost of generating additional random samples.

Sampling arrays: An array of non-normalized weights w_i (as from Equation 4) can be sampled by summing the weights and selecting the first item j where $\xi < \sum_j^n w_j / \sum_i^n w_i$.

Weighted reservoir sampling: Storing or recomputing all of the weights w_i to calculate the $1/\sum w_i$ normalization factor may be undesirable, especially on GPUs. Weighted reservoir sampling [Chao 1982] with sample reuse [Ogaki 2021] can be applied with weights generated sequentially. In this case, we skip normalization, sample j with probability proportional to w_i, and still apply Equation 5.

Positivization: Although negative weights can be sampled with probability based on their absolute value, doing so does not reduce variance as well as importance sampling of positive functions [Ernst et al. 2006]. All interpolating filters of a higher order than the linear filter have negative lobes and being able to estimate them with low variance is essential for stochastic texture filtering. We apply positivization [Owen and Zhou 2000], partitioning the filter weights w_i into positive (w_{i^+}) and negative (w_{i^-}) sets and sampling once from each set. The estimator of the filtered texture value of Equation 4 is

$$\langle F \rangle = W^+ \sum_i w_{i^+} t_{i^+} - W^- \sum_i w_{i^-} t_{i^-}. \tag{7}$$

The resulting positive and negative parts are not normalized and need to be weighted. We include an example of positivization used for the Mitchell bicubic filter in the supplementary material.

3 TEXTURE FILTERING AND RENDERING

Current practice in rendering is to filter textures before performing the lighting calculation, rather than applying the texture filter to the result of the lighting calculation. We start by formalizing the differences between those two approaches. In the following, we define $\hat{f}$ as the BSDF times the Lambertian cosine factor and parameterize it with the texture maps t^j that it depends on. Without loss of generality, we assume the same reconstruction filter f_r, low-pass filter f_l, and (u, v) parameterization for all textures.

With this notation, the traditional lighting integral that gives outgoing radiance L_o at a point p with texture coordinates (u, v) in direction ω_o is written:

$$L_\mathrm{o}(p, \omega_\mathrm{o}) = \int_{\mathbb{S}^2} \hat{f}\left(\omega_\mathrm{o}, \omega', (t^1 \otimes f_\mathrm{r} \otimes f_\mathrm{l})(u, v), \ldots\right) L_\mathrm{i}(p, \omega')\, \mathrm{d}\omega' \tag{8}$$

where the BSDF's parameters after the two directions are all filtered textures. We call this approach *filtering before shading*.

Alternatively, we may write the integral with the order of integration exchanged, convolving the outgoing radiance with one or both of the texture filters over its texture-space extent. With the low-pass filter applied after shading but the reconstruction filter applied before it, we have the *split-filtering shading* integral,

$$L_\mathrm{o}(p, \omega_\mathrm{o}) = \left[\int_{\mathbb{S}^2} \hat{f}\left(\omega_\mathrm{o}, \omega', (t^1 \otimes f_\mathrm{r})(u, v)), \ldots\right) L_\mathrm{i}(p, \omega')\, \mathrm{d}\omega'\right] \otimes f_\mathrm{l}. \tag{9}$$

Taking both filters outside the integral over the sphere gives the *filtering after shading* integral:

$$L_{\mathrm{o}}(p, \omega_{\mathrm{o}}) = \left[\int_{\mathbb{S}^2} \hat{f}\left(\omega_{\mathrm{o}}, \omega', t^1(u, v)), \ldots\right) L_{\mathrm{i}}(p, \omega')\, \mathrm{d}\omega' \right] \otimes f_{\mathrm{r}} \otimes f_{\mathrm{l}}. \tag{10}$$

If a texture makes an affine contribution to the lighting integral (i.e., is a linear term or a factor of it, such as a diffuse coefficient), then filtering before or after shading with Equation 8, 9, or 10 gives the same result since integration is a linear operator. For textures that make non-affine contributions (e.g., a normal map), the two differ. Filtering after shading eliminates systemic error in such cases (Figure 2, Section 3.1) and has the further benefit of reducing aliasing from high-frequency components of the shading function (Section 3.2).

Exact evaluation of Equations 9 and 10 can be costly. They reduce to sums just as Equation 3 does, but unlike texture filtering, the terms of these sums are costly to evaluate since they are not simple texel accesses. This cost may be reduced by sharing intermediate results between terms (e.g., the incident radiance function L_{i} or the result of tracing a shadow ray), though importance sampling algorithms may prefer different ray directions ω' for different terms due to varying BSDF parameters. At minimum, the BSDF must be evaluated for each term. As we will show in Section 4, these equations can be efficiently evaluated using stochastic sampling techniques.

Throughout the remainder of this paper, we will adhere to the filtering after shading formulation presented in Equation 10, unless stated otherwise.

3.1 Examples of Nonlinearities

Linear filtering of quantities that have a nonlinear effect on shaded results introduces bias and error in rendering. Examples include incorrect results from linear filtering of normal maps [Olano and Baker 2010] and nonlinear texture encodings like sRGB. Nonlinear quantities must be linearized for correct interpolation and minification [Microsoft 2015]. This insight dates to Reeves et al.'s work on percentage-closer shadow filtering (PCF), which showed that filtering depth values before performing shadow map lookups gives incorrect results while filtering visibility is effective [Reeves et al. 1987]. In their case, the binary visibility function is nonlinear (discontinuous step function). The "Future Work" section of their paper mentions the desirability of filtering other shading values, beyond visibility.

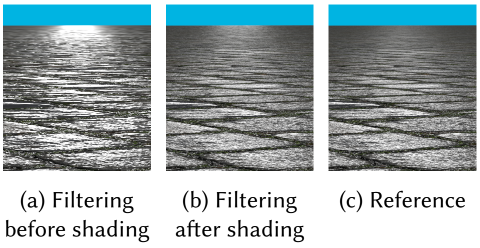
(a) Filtering before shading (b) Filtering after shading (c) Reference

Fig. 2. Appearance of a normal-mapped material under minification. Filtering before shading incorrectly filters the surface normal before shading, while filtering after shading more accurately reconstructs the material's appearance.

In this section, we show a few examples where filtering after shading gives a more accurate result than filtering before shading.

Normal maps. Linear filtering of normal maps leads to substantial changes in appearance [Olano and Baker 2010]. An example is shown in Figure 2(a), where hardware texture filtering is used on a minified normal-mapped surface. At points toward the horizon, the filter kernel is wide and filtering the normals gives values that are close to the average normal in the texture. Compared to the reference image in Figure 2(c), rendered with no lowpass filtering and at a higher resolution (through evaluation of many pixel samples), we see that filtering before shading introduces significant error. With filtering after shading, shown in Figure 2(b), results are much closer to the reference.

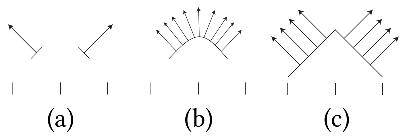

Fig. 3. (a) Two texels with normals nearly 90 degrees apart. (b) With bilinear filtering, a smooth distribution of normals is reconstructed. (c) Filtering after shading always uses single texel values from the image, so filters two discrete normals in this case.

With filtering after shading using Equation 10 only normals that are present in the normal map are used for lighting calculations. Thus, it can be understood as filtering discrete piecewise-linear microgeometry specified by the normal map, rather than using the normals to reconstruct a smooth underlying surface. Depending on the artist's intent, this behavior may or may not be desirable—consider the example shown in Figure 3 where adjacent texels have significantly-different normals. With bilinear filtering, the filtered normals vary smoothly, corresponding to a smooth underlying surface, while filtering after shading blends the results of shading discrete normals. If the former behavior is desired, the split filtering integral of Equation 9 may be used in an alternative to Equation 10 in such cases.

Filtering of discrete quantities. Filtering BRDF properties prior to shading may violate the physical constraints of a BRDF model. Consider a texture used for a scalar "metalness" parameter for a physically-based material model, where only the values 0 and 1 have physical meaning. With filtering after shading, the material is only evaluated with metalness values of 0 and 1. At areas where the texture filter spans both values, the material itself is filtered, only using one of those two values. With traditional texture filtering and split-filtering shading with Equation 9, metalness values between 0 and 1 result, which may be nonsensical and produce visual error, depending on the material model.

Filtering nonlinear physical properties. We show another example in Figures 4(a) and (b), where a grid of temperature values is used to describe the full emission spectrum using Planck's law, which is nonlinear. With the filtering before shading, averaged temperature values are used to compute the emission spectrum. In contrast, filtering after shading computes emission spectra at the grid points and then filters those spectra; it thus preserves appearance under minification, while filtering the temperatures does not. Figure 4(c) shows the error introduced when volumetric prefiltered MIP maps are used for minification. Filtering after shading (here, with a Gaussian in the plane perpendicular to the ray), preserves appearance under minification, Figure 4(d).

3.2 Nonlinearity-Introduced Aliasing

While filtering after shading gives superior results in many cases, it can either reduce or amplify aliasing. Nonlinearities in the lighting calculation always introduce high frequencies that are not present in the material texture. In discrete signals, those additional high frequencies can exceed the original Nyquist limit and alias irrecoverably. We describe and analyze this effect from a signal processing perspective in the supplemental material (Section S.3).

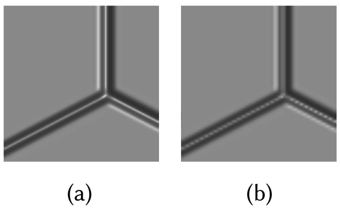

Fig. 5. A magnified normal-mapped specular surface. (a) Traditional filtering. (b) Filtering after shading with Equation 10 introduces aliasing.

Reordering the texture filtering computation changes the rate at which nonlinearity is introduced. When filtering after shading, the nonlinearity is introduced at the texture resolution. Conversely, when filtering before shading, the nonlinearity is introduced at the screen resolution. Under minification, the screen resolution is lower than the

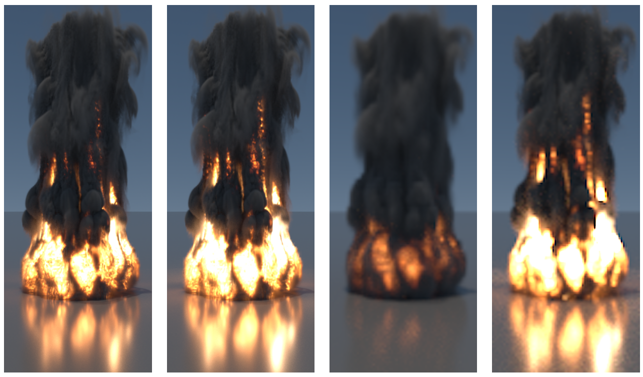
(a) Filtering before shading
(b) Filtering after shading
(c) Minification, with filtering before shading
(d) Minification, with filtering after shading

Fig. 4. (a) The traditional approach filters first, then uses Planck's law to compute the volumetric emission spectrum. In contrast, (b) filtering after shading filters the emission spectra given by Planck's law. Because Planck's law is highly nonlinear, the results differ. Under minification, (c) MIP mapping introduces error by applying linear filtering to nonlinear quantities. Appearance is accurately preserved with (d) filtering after shading and no MIP maps.

texture resolution and filtering after shading reduces aliasing (Figure 2). Under magnification, the screen resolution is higher than the texture resolution.

When filtering after shading in this case, shading can introduce aliasing in the lower texture resolution (Figure 5). In practice, the severity of this effect depends on the spectral contents of the filtered textures, the magnification factor, and how nonlinear the shading is. For example, very glossy specular surfaces introduce significantly higher spatial frequencies.

4 STOCHASTIC TEXTURE FILTERING

We introduce Stochastic Texture Filtering (STF)—stochastic estimation of the filtering after shading that makes evaluating the split-filtering and filtering-after-shading equations computationally efficient. Expanding the outer convolution in Equation 9 gives:

$$L_{\mathrm{o}}(p) = \int f_{\mathrm{l}}(u', v') \left[\int_{\mathbb{S}^2} \hat{f}\left(\omega_{\mathrm{o}}, \omega', (t^1 \otimes f_{\mathrm{r}})(u', v')), \ldots\right) L_{\mathrm{i}}(p, \omega')\, \mathrm{d}\omega' \right] \mathrm{d}u' \mathrm{d}v'. \tag{11}$$

If (u', v') samples are drawn with probability proportional to the low-pass filter f_{l}, then the standard Monte Carlo estimator gives:

$$L_{\mathrm{o}}(p, \omega_{\mathrm{o}}) \approx \int_{\mathbb{S}^2} \hat{f}\left(\omega_{\mathrm{o}}, \omega', (t^1 \otimes f_{\mathrm{r}})(u', v')), \ldots\right) L_{\mathrm{i}}(p, \omega')\, \mathrm{d}\omega', \tag{12}$$

which stochastically samples the minification filter but still explicitly evaluates the reconstruction filter. Alternatively, applying Monte Carlo to Equation 10 gives the estimator:

$$L_{\mathrm{o}}(p, \omega_{\mathrm{o}}) \approx \int_{\mathbb{S}^2} \hat{f}\left(\omega_{\mathrm{o}}, \omega', t^1_{u',v'}, \ldots\right) L_{\mathrm{i}}(p, \omega')\, \mathrm{d}\omega', \tag{13}$$

where a single texel is sampled.

4.1 Filter Reservoir Sampling (FRS)

The texture filter can be sampled by evaluating its weight at all of the (u, v) texel coordinates under its extent and then sampling a (u', v') with probability proportional to these weights. To avoid the need to store all of these values, we use the weighted reservoir sampling technique. We call this combination of techniques *Filter Reservoir Sampling (FRS).*

As an example, consider the multidimensional B-spline filter K_{bs} defined as a product of 1D cubic B-splines. In 2D, given a lookup point $(u, v) \in \mathbb{R}^2$, the filtered shading value is given by 4×4 weighted texel values:

$$\sum_{i=-1}^{2} \sum_{j=-1}^{2} K_{\text{bs}}(\lfloor u \rfloor + i)\, K_{\text{bs}}(\lfloor v \rfloor + j) \left[\int_{\mathbb{S}^2} \hat{f}\left(\omega_{\text{o}}, \omega', t^1_{\lfloor u \rfloor + i, \lfloor v \rfloor + j}, \ldots\right) L_{\text{i}}(p, \omega')\, \mathrm{d}\omega' \right]. \tag{14}$$

The filter is separable so we can apply weighted reservoir sampling to each dimension independently. For example, for u', we sample $i' \in [-1, 0, 1, 2]$ according to the weights $K_{\text{bs}}(\lfloor u - 1 \rfloor)$, $K_{\text{bs}}(\lfloor u \rfloor)$, $K_{\text{bs}}(\lfloor u + 1 \rfloor)$, and $K_{\text{bs}}(\lfloor u + 2 \rfloor)$. The single texel value at (u', v') can then be used in the shading computation to produce an unbiased estimate of Equation 10. Sampling higher-dimensional B-spline filters follows the same approach; for an n-dimensional filter, 4^n texture lookups are replaced with a single one. Separable sampling reduces the sample selection cost from 4^n to $4n$.

Our implementation of stochastic elliptically weighted average filtering is also based on reservoir sampling: after stochastically selecting a MIP level based on the ellipse's extent, we then compute all of the EWA filter weights and sample one based on their distribution.

4.2 Filter Importance Sampling (FIS)

It is also possible to stochastically sample continuous filters without discretizing them using a technique based on *filter importance sampling* (FIS) [Ernst et al. 2006; Reeves et al. 1987; Shirley 1990]. However, it is not possible to directly apply FIS to the filtering after shading integral, Equation 10, since FIS assumes the integration of a product of two continuous functions. In this case, the texture functions $t(u, v)$ are zero everywhere except at discrete texel coordinates (recall Equation 1), so sampled (u', v') coordinates have zero probability of finding a texture sample. If a continuous texture function is defined using a reconstruction filter, however, then FIS can be applied.

A natural choice for the texture reconstruction filter f_{f} is the n-dimensional unit box filter $[-1/2, 1/2]^n$. In turn, after a (u', v') is sampled from the texture filter f, applying nearest-neighbor sampling is equivalent to applying the box filter. Introducing the nearest-neighbor reconstruction filter corresponds to convolving the original filter function f with a box filter, changing its shape. Hence, the filter function that is sampled should be the deconvolution of the desired filter with the box function.[2]

We can thus filter with a B-spline filter of degree n by sampling a spline of degree $n - 1$ and performing a nearest lookup, since approximating B-splines are constructed by repeated convolution of a box filter via the Cox–de Boor recursion formula [De Boor 1977]. (For example, a quadratic approximating B-spline filter can be realized by sampling a triangular PDF over $[-1.5, 1.5]^2$.) Sampling can either be performed via CDF inversion or by adding n uniformly-distributed random variables (also following the Cox–de Boor recursion).

Filter importance sampling is appealing for stochastic texture filtering since it allows for filters with infinite spatial support and has a cost that is independent of the filter's width. It can be

[2]This perspective allows us to better understand Hofmann et al.'s stochastic trilinear sampling algorithm, which is based on independent, uniform jittering in each dimension and then nearest neighbor sampling [Hofmann et al. 2021]. Their jittering corresponds to applying FIS to sample the box filter which is then convolved with another box function, giving their stochastic trilinear interpolant.

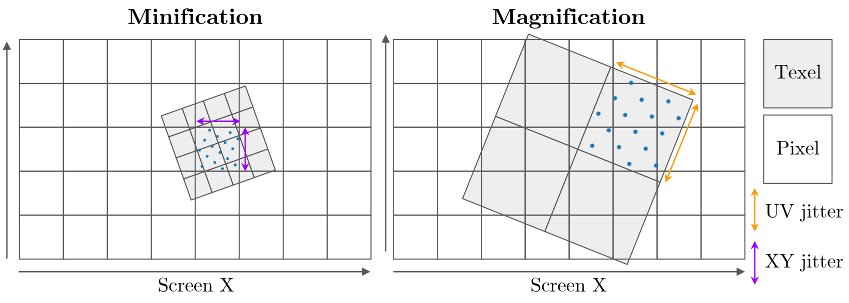

Fig. 6. Image reconstruction filter screen-space jittering (**left**) and UV space filter importance sampling jittering (**right**). During magnification, the spatial extent of the screen-space jitter can be significantly smaller than a texel size, which can cover multiple pixels. For the texture reconstruction filter f_f larger magnitude jitters are necessary.

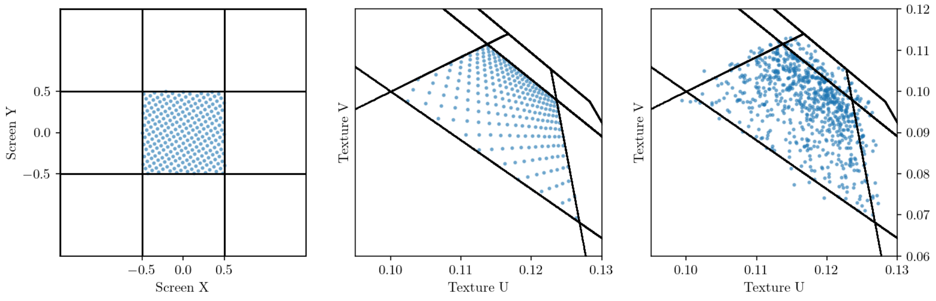

Fig. 7. Uniform jittering in screen-space within pixel bounds (**left**) produces trapezoid, non-uniform coverage in the UV texture space (**middle**). Filter importance sampling then *additionally* jitters the resulting UVs in texture space for a desired texture reconstruction filter f_f (Section 4.2), for example with Gaussian distribution (**right**).

used with positivization (Section 2.2) for low variance evaluation of filters with negative lobes. Filter importance sampling a screen-space reconstruction filter is a common practice in production renderers. It can effectively approximate a minification low-pass filter, such as an anisotropic filter (Figure 7 left and middle). However, it is not enough to rely on screen-space jittering for magnification, as the magnitude is too small (Figure 6) and it produces nearest-neighbor interpolated texture. We propose to use FIS for texture reconstruction and sampling in addition to screen-space reconstruction filtering jitter.

4.2.1 Screen-Space Anisotropic Minification. Anisotropic filtering techniques commonly model the filter footprint as an ellipse, with axes derived from the partial derivatives of texture coordinates relative to screen coordinates. To save computational cost, similarly to Lee et al. [Lee et al. 2017] we do not sample the ellipse in the shader but rely on screen-space jittering within the pixel to approximately sample the same extent. As shown in Figure 7, uniform jittering within the pixel gives a trapezoidal shape and projection in UV space. Although this does not preserve area or the original sample point distribution, it has no additional computational cost and in our experiments, approximates anisotropic filtering well.

The degree of anisotropy is determined by the ratio between the major and minor axes of the ellipse. We choose a MIP level based on the length of the minor axis and sample a single MIP level

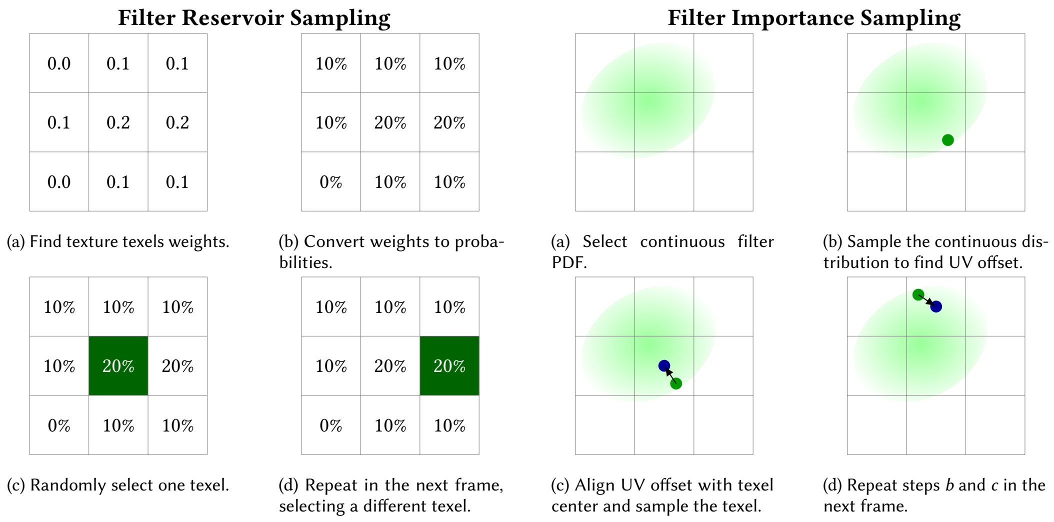

(a) Find texture texels weights.
(b) Convert weights to probabilities.
(c) Randomly select one texel.
(d) Repeat in the next frame, selecting a different texel.

(a) Select continuous filter PDF.
(b) Sample the continuous distribution to find UV offset.
(c) Align UV offset with texel center and sample the texel.
(d) Repeat steps *b* and *c* in the next frame.

Fig. 8. Comparison of two magnification filtering stochastic texture mapping methods. Note that with Filter Importance Sampling, the final filter is the result of convolving the sampled distribution with the texel extent box filter.

stochastically. Unlike current GPU hardware filtering, which has a maximum anisotropy ratio of 16, our method allows any anisotropy. We limit the ratio to 64 to avoid GPU texture cache thrashing, rescaling the minor axis if necessary. This approach of combining screen-space jittering with a higher-resolution MIP selection is similar to the ad-hoc practice of *negative MIP biasing* [Karis 2014; Yang et al. 2020] used in contemporary rendering engines for improved texture sharpness and reduced shading aliasing. We combine the screen-space jittering with either discrete filter sampling or UV jittering filter importance sampling (Figure 7).

We note that using MIP maps with stochastic texture filtering introduces an error since MIP maps encode prefiltered texture values. Therefore, the technique as described is no longer filtering after shading, but a hybrid between filtering before and after shading. The choice of MIP map defines the degree to which the textures are prefiltered and the resulting error. This error can be reduced by using finer levels of the MIP chain, which can be achieved by applying a negative LOD bias or by increasing the maximum amount of anisotropy. Alternatively, the error can be minimized by generating MIP levels using an appearance-driven approach [Hasselgren et al. 2021]. If increased required memory bandwidth is not a concern, the error can be eliminated by not using MIP mapping at all. We find that this error is usually not objectionable in practice; compare for example Figures 9 (f) and (g), where the first uses MIP mapping and the second always samples the finest MIP level. Both are nearly the same as the reference image, (h).

4.3 Comparison of FRS and FIS

FIS and FRS are graphically compared in Figure 8. Both approaches are straightforward to execute, though for many filters, FIS is significantly easier to implement and requires fewer arithmetic operations to evaluate. (We provide code examples of both in the supplementary material.) Unlike FRS, the cost of filter importance sampling is constant and does not depend on the filter size, including filters with infinite spatial support. The Gaussian convolutional filter is an example of an infinite filter; although it is often truncated in practice, with FIS it is possible to evaluate it without

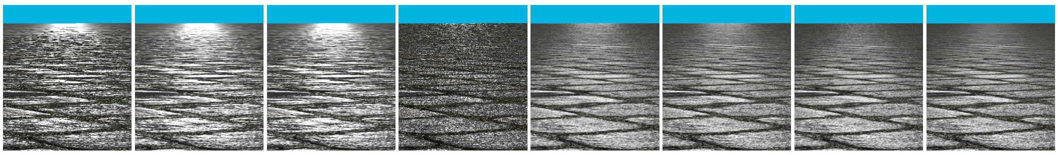
(a) Filter Before 1 spp
(b) Filter Before 1 spp + DLSS
(c) Filter Before 1024 spp
(d) Filter After 1 spp
(e) Filter After 1 spp + DLSS
(f) Filter After 1024 spp
(g) Filter After LOD 0, 1 spp, DLSS
(h) Reference 1024 spp

Fig. 9. Appearance of a normal-mapped surface under minification. (a)–(c) use filtering before shading with hardware texture filtering, MIP maps, and a maximum anisotropy of 16. (d)–(g) use filtering after shading with a stochastic bicubic filter and a maximum anisotropy of 64. MIP maps are used in (d)–(f), while (g) uses no MIP maps. (h) is a point sampled reference image. All variants of filtering after shading more accurately preserve the material's appearance, while traditional texture filtering introduces significant error.

truncation. This can simplify implementation (it is not necessary to carefully window the filter), as well as save the computational cost of multiple discrete weight evaluations and sample selection.

The box reconstruction filter introduced in filter importance sampling can be useful for rapidly changing filters such as a small-sigma Gaussian: evaluating it at discrete points results in subsampling error [Wronski 2021] and the correction requires evaluating the costly *erf* error function. Filter importance sampling an analytical normal distribution produces the same effect due to the convolution of a nearest-neighbor box function with the Gaussian.

The cases where FRS is preferred over FIS include applications where the filter is given only in a discrete form (such as convolutional neural networks). Also, some continuous filters are difficult to sample due to the lack of closed-form PDF sampling procedure. Similarly, filters with negative lobes are significantly more difficult to sample with FIS. Finally, FIS requires multiple random numbers and it is easier to preserve stratification with FRS.

4.4 Material Graphs

Complex patterns are often generated using graphs composed of simple nodes, with textures at the leaves. In offline rendering, it is not uncommon for these graphs to have hundreds of nodes and use many source textures, each of which is filtered at each shading point. Linear combinations of textures can be evaluated stochastically using Equation 5 and more complex blends such as triplanar mapping, based on a blend of three textures weighted by the orientation of the surface, can also be sampled stochastically.

5 RESULTS

We have evaluated stochastic texture filtering in the context of both real-time rasterization and path tracing using *Falcor* [Kallweit et al. 2022], as well as offline rendering using *pbrt-v4* [Pharr et al. 2022]. All performance measurements were taken on an NVIDIA RTX 4090 GPU.

We evaluate stochastic texture filtering in a real-time renderer, using DLSS [Liu 2022] as a robust temporal integrator. Screen-space jittering for DLSS employs a 32-sample Halton sequence, while Spatio-Temporal Blue Noise (STBN) masks [Wolfe et al. 2022] are used as the source of random numbers for stochastic filtering. Our implementation performs stochastic filtering in the shading pass, which uses the Disney BRDF [Burley 2012] and a single directional light. All real-time images and performance measurements were taken at 4K (3840×2160) resolution.

Unlike software (CPU) renderers, real-time rendering with GPUs can use the hardware texturing unit with excellent bilinear filtering performance on standard texture formats. We do not expect stochastic texture filtering to provide performance benefits with those formats when magnifying

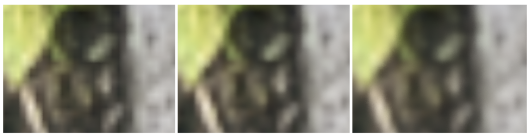

Fig. 10. Bilinear filtering (a) compared to stochastic, single sample estimation of the bicubic Mitchell (b) and Gaussian (c) filters, resolved with DLSS's temporal accumulation. The Mitchell filter is much sharper than the bilinear and does not produce diamond-like artifacts. The Gaussian filter is isotropic and although it tends to blur textures, it gives the best results for reconstruction of diagonal lines.

textures. We show, however, that it allows for efficient and high-performance use of novel texture representation and compression formats not supported by existing hardware, as well as optimization of material graphs. Furthermore, we demonstrate how stochastic texture filtering enables magnification filters of significantly higher quality than the bilinear filter at the same cost, and more correct appearance preservation and minification.

Filtering After Shading: We present a combined effect of stochastic magnification and minification on Figure 9. Since we do not fully supersample the source texture, but still use MIP maps (Section 4.2.1) our proposed stochastic filters introduce a small error, visible by comparing Figure 9(e) and (g). Figure 9(g) uses only the most detailed MIP level. All variants of STF are closer to the reference than the filtering before shading approach.

Magnification, Filter Reservoir Sampling: For magnification, we analyze the visual benefits of high-quality bicubic Mitchell and Gaussian filters with stochastic texture filtering by comparing with a bilinear filter, which is known for producing diamond-like artifacts and over-blurring. While the implementation of the stochastic Gaussian filter is straightforward, the Mitchell filter has negative weights and so we apply positivization (Section 2.2), which doubles the cost of stochastic filtering. In Figure 10 we observe better image quality from the higher-quality filters: either sharper response without bilinear filtering artifacts, or more pleasant diagonal edges and image smoothness. The use of STBN and DLSS results in no objectionable noise or flicker.

Magnification, Filter Importance Sampling: Filter importance sampling allows to use infinite-extent filters without truncation. We compare FIS to FRS using three Gaussian filters in Figure 11. For FRS, we choose a single sample in the closest 4×4 window of texels and for FIS, we use the Box–Muller transform to sample the Gaussian, followed by a nearest-neighbor lookup.

Results are visually indistinguishable for $\sigma = 0.5$ but differ for the two other sigmas. With a very small σ, we observe undersampling with discrete sample weights. For the large σ, the limited radius of discrete sampling truncates the Gaussian kernel and produces subtle, grid-like visual artifacts. This can be improved by enlarging the filtering window, with a corresponding increase in the cost of sampling. FIS does not suffer from either of those issues, though it requires two random variables and cannot filter with exact kernels when additional convolution with a box filter is not desirable.

Anisotropic filtering and minification: Lowpass filtering is more difficult to resolve than reconstruction filtering, as it needs to average significantly more samples. We verify that the commonly used temporal filter, DLSS, can resolve it in Figure 12. We use a plane textured with a challenging, high-contrast checkerboard pattern. The image reconstructed by DLSS is temporally stable, with occasional flickering in regions containing very high-frequency details. In motion, we observe sporadic ghosting and other temporal artifacts introduced by DLSS, but the overall image quality remains comparable to hardware anisotropic filtering. We present those results in the supplementary video. Although DLSS does not completely remove noise caused by stochastic

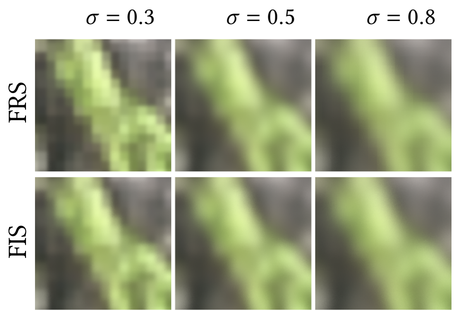

Fig. 11. Gaussian texture filtering with varying σ, comparing FRS and FIS. For $\sigma = 0.5$, both produce very similar results. FIS gives better results for both relatively small and large σ. We encourage the reader to zoom in to see the difference in the last column.

texture sampling on such a high-contrast pattern, STBN reduces it, making it barely perceptible and only in magnified areas. Figure 9 also demonstrates that temporal reconstruction is effective in recovering a high-quality anisotropically filtered image while only using 1 spp.

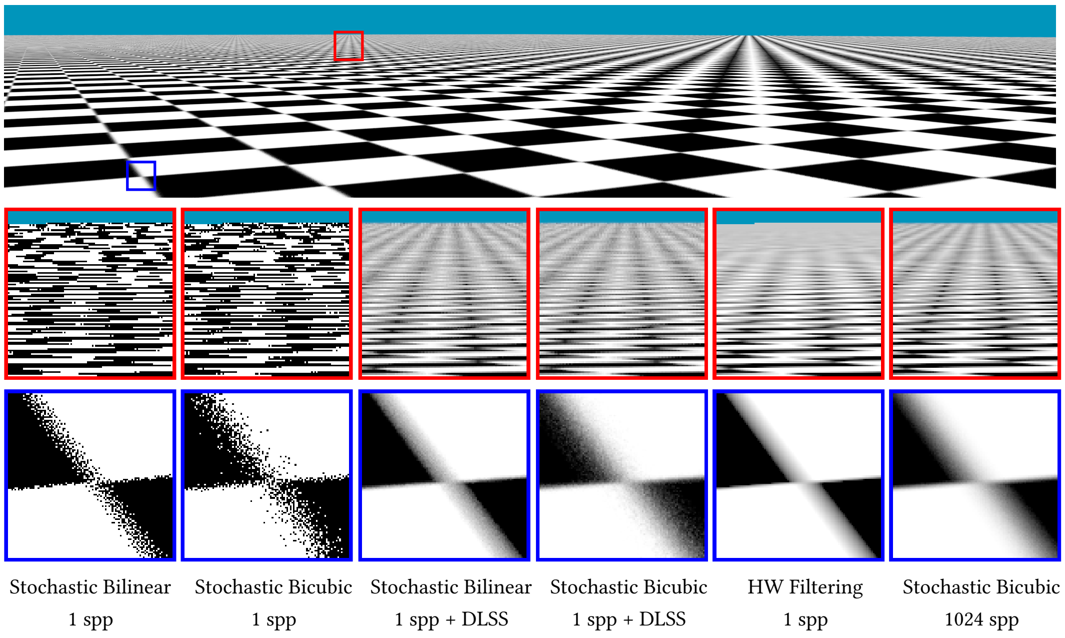

Fig. 12. A checkerboard rendered using stochastic anisotropic and bicubic filtering (**top**). Red and blue insets (**bottom rows**) show minified and magnified areas, respectively, comparing stochastic bilinear and bicubic filtering with hardware anisotropic filtering and a 1024 spp reference solution. Stochastic filtering uses FIS with STBN, except for the reference image that used a uniform distribution for the filtering.

Triplanar mapping: Triplanar mapping samples all textures three times with UV coordinates aligned to the *XY*, *XZ*, and *YZ* planes and blends the filtered results based on the surface normal direction to avoid excessive texture stretching. Since it is a weighted average of three values, we can evaluate it stochastically using Equation 5. Results are shown in Figure 13. We find that

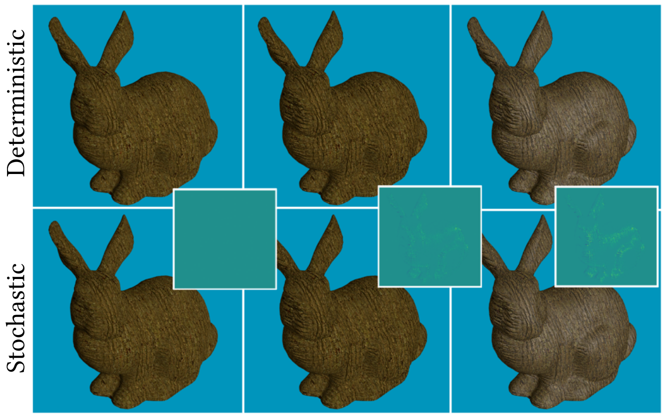

Fig. 13. Full triplanar mapping (**top**) compared to its stochastic, single sample estimation (**bottom**). From left to right we present pure diffuse shading without normal mapping, diffuse shading with normal mapping, and full specular and diffuse lighting. Insets show error magnified 10×.

DLSS resolves the stochastic sampling error effectively and observe no temporal visual artifacts such as flicker or ghosting. The difference for the diffuse-only case comes from the use of the temporal reconstruction filter, as filtering before and after shading is mathematically equivalent. For normal-mapped and specular surfaces, filtering after shading is different than filtering before shading, but in this scene, the visual differences after shading are minor.

Texture compression: Stochastic texture filtering enables the use of more advanced texture compression and decompression algorithms by requiring only a single texel to be decoded at each lookup [Hofmann et al. 2021; Vaidyanathan et al. 2023]. To connect those observations to our work, we implemented a much simpler real-time decompression algorithm—the 2D discrete cosine transform (DCT), where 8×8 texel blocks store only 4 bytes per channel. We store the six lowest-frequency DCT coefficients for each channel, allocating 7 bits for the DC component and 5 bits for the remaining coefficients, achieving 16× compression for 8-bit data. Texel values must be decoded in the material evaluation shader and filtering must be performed manually.

As shown in Figure 14, stochastic trilinear filtering gives nearly identical visual results to deterministic trilinear filtering and measure a 2.9× performance improvement. To further demonstrate the applicability of the proposed methods, we combine it with stochastic triplanar mapping, yielding a total 7.9× performance improvement as compared to fully-deterministic filtering.

Visual noise ablation study: To validate the effectiveness of DLSS [Liu 2022] as the temporal integrator and Spatio-Temporal Blue Noise (STBN) [Wolfe et al. 2022] as the source of the randomness, we performed an ablation study presented in Figure 15 and using extreme zoom-in on a high contrast area. We verify that as compared to white noise, STBN dramatically reduces the appearance of noise and improves its perceptual characteristics. Similarly, DLSS removes most of the noise—both in the case of white noise and STBN. When DLSS is used in combination with white noise, some visual grain remains, but it disappears completely when combined with STBN.

Offline-Rendering: In order to evaluate the error introduced by stochastic filtering when used with volumetric path tracing, we rendered a view of the *Disney Cloud* [Walt Disney Animation Studios 2017]. *pbrt*'s volumetric path tracer is based on delta tracking with null scattering [Kutz et al. 2017; Miller et al. 2019] and uses ratio tracking [Novák et al. 2014] for transmittance. Because the cloud's density is used to scale the absorption and scattering coefficients and since those make

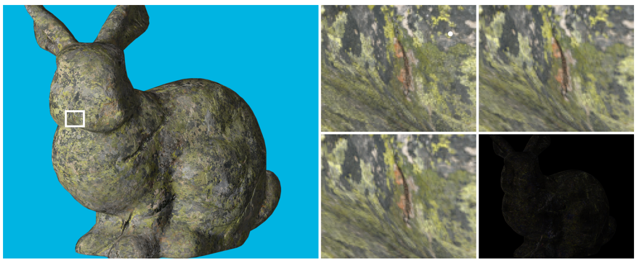

Fig. 14. Stochastic filtering of a DCT-compressed texture set (**left**). Despite some loss of higher frequency details in the original uncompressed texture (**upper left inset**), the stochastic trilinear (**upper right inset**) and deterministic trilinear (**lower left inset**) filtering results appear virtually identical, as shown by the 10× magnified error image (**bottom right**). Stochastic filtering reduces rendering time from 1.66 ms to 0.57 ms.

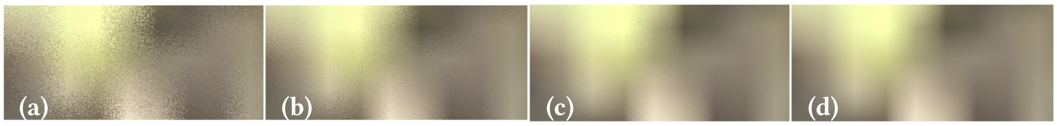

Fig. 15. Effectiveness of DLSS and STBN on noise removal in a real-time setting. White noise (**a**) creates visually distracting patterns of noise, while STBN (**b**) dramatically reduces its appearance. When using DLSS as a temporal integrator (**c**) noise is dramatically reduced as compared to a single frame result (**a**). DLSS and STBN combined (**d**) make the noise almost imperceptible.

affine contributions to the estimated radiance values, both filtering approaches converge to the same result.

We converted the OpenVDB data set to NanoVDB for use on the GPU and used the 8× down-sampled version of the cloud in order to make the visual difference between filters more apparent. The image in Figure 1 was rendered at 1080p resolution with 256 samples per pixel (spp). Trilinear filtering causes block- and diamond-shaped artifacts that are not present with tricubic filtering. Stochastic filtering gives images that are visually indistinguishable from traditional filtering; the error it introduces is far less than the error from Monte Carlo path tracing. For this scene, we saw less than a 5% increase in mean squared error (MSE) due to the stochastic filters. Compared to trilinear filtering, tricubic filtering doubles rendering time since it requires 8× more texel lookups in the NanoVDB multilevel grid. With stochastic filtering, we can render using a high-quality tricubic filter in less time than trilinear filtering, with 1/8 as many texel lookups.

6 RECOMMENDATIONS

While we believe that filtering after shading is more correct for most nonlinear operations and textures, we note that the change of filtering order presents a practical challenge. Different filtering methods may produce varying results, even if their lighting and material systems are the same. It means that our method could change the appearance of existing 3D assets and require an art review before being used as a replacement.

We note that filtering after shading is visually indistinguishable from filtering before shading for mostly diffuse or rough surfaces. Higher degrees of non-linearity present in shading such as transparency can cause significant deviations in appearance—for instance, alpha testing becomes stochastic transparency, which may or may not be desired. Furthermore, our proposed framework works best when there is enough spatiotemporal data to reconstruct the shaded surfaces. Even the most sophisticated machine-learning-based reconstruction techniques break down with subpixel geometric detail that flickers from frame to frame. This can result in excessive noise, flicker, or blurring, depending on the used algorithm.

Filtering after shading and STF work especially well for minification and reduce aliasing. Rendering non-linearity introduces new high-frequency content at high texture resolution, which can be efficiently filtered over multiple pixels or samples. Swapping the order of filtering during magnification can instead enhance aliasing caused by nonlinearities applied at lower resolutions, as shown in Figure 5.

If the magnification factors are large, rendering is highly nonlinear, and textures contain high-frequency content, stochastic magnification can yield subjectively poorer results. This problem can be addressed by maintaining a close 1-to-1 texel-to-pixel ratio and limiting magnification factors. With the ubiquity of texture streaming and virtual texturing, this can be achieved with sufficient disk storage, or through upsampling and generative techniques during texture streaming.

7 DISCUSSION AND FUTURE WORK

We have shown that stochastic texture filtering allows efficiently filtering outside of the lighting integral, rather than first filtering the texture parameters used by it. By doing so, systematic error is eliminated from rendered images in the common case where a textured parameter has a non-affine contribution to the final result during minification. Examples include normal mapping, many BSDF properties, and temperatures mapped to emission spectra. Filtering lighting preserves appearance at different scales.

Stochastic filtering offers additional benefits, including making complex compressed texture representations viable by reducing filters to a single texel lookup. It allows the use of higher-quality texture filters in high-performance code, as we have shown with bicubic and Gaussian filters, providing further improvements in image quality. We hope that our work will contribute to the adoption of higher-order texture filters in real-time rendering and reduce the reliance on low-quality bilinear filters.

We demonstrated that the minor noise introduced by stochastic texture filtering can be effectively managed using temporal filtering algorithms like DLSS. While the overall reconstruction quality is satisfactory, minor flickering and ghosting artifacts remain, especially in high-contrast areas and patterns like a checkerboard. DLSS is a learning-based solution and was not trained on data that includes stochastic texture filtering. Including stochastically filtered inputs in the training datasets would likely further improve the reconstruction quality.

Finally, our approach makes it feasible to use more complex, non-linear reconstruction filters, such as steering or bilateral kernels. Such filter can be effective at reconstructing features like edges in images [Takeda et al. 2007] and volumes [Yu and Turk 2013] and are essential for super-resolution. If such nonlinear, local filter parameters or weights can be obtained cheaply (for example, computed at a lower resolution [Wronski et al. 2019]), our stochastic filtering framework could be applied to them, giving further improvements to image quality.

ACKNOWLEDGMENTS

We would like to thank Aaron Lefohn and NVIDIA for supporting this work, John Burgess for suggesting the connection to percentage closer filtering, Karthik Vaidyanathan for many discussions and suggestions, Johannes Deligiannis for finding the problem with nonlinearity introduced aliasing, Markus Kettunen for comments about texture reconstruction versus low-pass filtering, and Tomas Akenine–Möller for helpful comments on a draft of this paper. We thank the wide graphics community on social media for discussion and historical references to the earliest uses of stochastic texture filtering in video games. We are grateful to Walt Disney Animation Studios for making the detailed cloud model available and to Lennart Demes, author of the *ambientCG* website, for providing a public-domain PBR material database that we used to produce the real-time rendering figures.

REFERENCES

Tomas Akenine-Möller, Cyril Crassin, Jakub Boksansky, Laurent Belcour, Alexey Panteleev, and Oli Wright. 2021. Improved Shader and Texture Level of Detail Using Ray Cones. *Journal of Computer Graphics Techniques (JCGT)* 10, 1 (25 January 2021), 1–24. http://jcgt.org/published/0010/01/01/

Anthony C. Barkans. 1997. High Quality Rendering Using the Talisman Architecture. In *Proceedings of the ACM SIGGRAPH/EUROGRAPHICS Workshop on Graphics Hardware* (Los Angeles, California, USA). 79–88. https://doi.org/10.1145/258694.258722

Colin Barré-Brisebois, Henrik Halén, Graham Wihlidal, Andrew Lauritzen, Jasper Bekkers, Tomasz Stachowiak, and Johan Andersson. 2019. Hybrid Rendering for Real-time Ray Tracing. *Ray Tracing Gems: High-Quality and Real-Time Rendering with DXR and Other APIs* (2019), 437–473.

James F. Blinn and Martin E. Newell. 1976. Texture and Reflection in Computer Generated Images. *Commun. ACM* 19, 10 (Oct. 1976), 542–547. https://doi.org/10/dct2v6

Brent Burley. 2012. Physically-Based Shading at Disney. In *Practical Physically-Based Shading in Film and Game Production*. 10:1–10:7.

R. J. Cant and P. A. Shrubsole. 2000. Texture Potential MIP Mapping, a New High-Quality Texture Antialiasing Algorithm. *ACM Trans. Graph.* 19, 3 (July 2000), 164–184. https://doi.org/10.1145/353981.353991

Edwin E. Catmull. 1974. *A Subdivision Algorithm for Computer Display of Curved Surfaces*. Ph. D. Dissertation. Dept. of CS, U. of Utah.

Min-Te Chao. 1982. A General Purpose Unequal Probability Sampling Plan. *Biometrika* 69, 3 (Dec. 1982), 653–656. https://doi.org/10/fd87zs

Petrik Clarberg, Simon Kallweit, Craig Kolb, Pawel Kozlowski, Yong He, Lifan Wu, Edward Liu, Benedikt Bitterli, and Matt Pharr. 2022. Real-Time Path Tracing and Beyond. HPG 2022 Keynote.

Carl De Boor. 1977. Package for calculating with B-splines. *SIAM J. Numer. Anal.* 14, 3 (1977), 441–472.

Claude E Duchon. 1979. Lanczos filtering in one and two dimensions. *Journal of Applied Meteorology and Climatology* 18, 8 (1979), 1016–1022.

Eric Enderton, Erik Sintorn, Peter Shirley, and David Luebke. 2010. Stochastic transparency. In *Proceedings of the ACM SIGGRAPH Symposium on Interactive 3D Graphics and Games*. 157–164.

Manfred Ernst, Marc Stamminger, and Günther Greiner. 2006. Filter Importance Sampling. In *Proceedings of IEEE Symposium on Interactive Ray Tracing*. 125–132. https://doi.org/10/c2q6gj

Alejandro Conty Estevez and Christopher Kulla. 2018. Importance Sampling of Many Lights with Adaptive Tree Splitting. *Proceedings of the ACM on Computer Graphics and Interactive Techniques* 1, 2 (Aug. 2018), 25:1–25:17. https://doi.org/10/ggh89v

Iliyan Georgiev and Marcos Fajardo. 2016. Blue-Noise Dithered Sampling. In *ACM SIGGRAPH Talks*. ACM Press, 35:1–35:1. https://doi.org/10/gfznbx

Ned Greene and Paul S. Heckbert. 1986. Creating Raster Omnimax Images from Multiple Perspective Views Using the Elliptical Weighted Average Filter. *IEEE Computer Graphics and Applications* 6, 6 (1986), 21–27. https://doi.org/10.1109/MCG.1986.276738

Larry Gritz. 2022. OpenImageIO 2.4. https://github.com/OpenImageIO/oiio/releases/tag/v2.4.4.1

Yu Guo, Miloš Hašan, and Shuang Zhao. 2018. Position-Free Monte Carlo Simulation for Arbitrary Layered BSDFs. *ACM Transactions on Graphics (Proceedings of SIGGRAPH Asia)* 37, 6 (Dec. 2018), 279:1–279:14. https://doi.org/10/db3c

Jon Hasselgren, Jacob Munkberg, Jaakko Lehtinen, Miika Aittala, and Samuli Laine. 2021. Appearance-Driven Automatic 3D Model Simplification. In *Eurographics Symposium on Rendering*.

Paul Heckbert. 1989. *Fundamentals of Texture Mapping and Image Warping*. Ph. D. Dissertation. UC Berkeley.

Paul S. Heckbert. 1986. Survey of Texture Mapping. *IEEE Computer Graphics and Applications* 6, 11 (1986), 56–67. https://doi.org/10.1109/MCG.1986.276672

Eric Heitz, Johannes Hanika, Eugene d'Eon, and Carsten Dachsbacher. 2016. Multiple-Scattering Microfacet BSDFs with the Smith Model. *ACM Transactions on Graphics (Proceedings of SIGGRAPH)* 35, 4 (July 2016), 58:1–58:14.

Nikolai Hofmann, Jon Hasselgren, Petrik Clarberg, and Jacob Munkberg. 2021. Interactive Path Tracing and Reconstruction of Sparse Volumes. *Proc. ACM Comput. Graph. Interact. Tech.* 4, 1, Article 5 (April 2021), 19 pages. https://doi.org/10.1145/3451256

Homan Igehy. 1999. Tracing Ray Differentials. In *Proceedings of the 26th Annual Conference on Computer Graphics and Interactive Techniques (SIGGRAPH '99)*. ACM Press/Addison-Wesley Publishing Co., USA, 179–186. https://doi.org/

10.1145/311535.311555

Productions Interplay. 1992. Texture Scaling in Star Trek: 25th Anniversary. https://st25sprites.neocities.org/scaling

James T. Kajiya. 1986. The Rendering Equation. *Computer Graphics (Proceedings of SIGGRAPH)* 20, 4 (Aug. 1986), 143–150. https://doi.org/10/cvf53j

Simon Kallweit, Petrik Clarberg, Craig Kolb, Tom'aš Davidovič, Kai-Hwa Yao, Theresa Foley, Yong He, Lifan Wu, Lucy Chen, Tomas Akenine-Möller, Chris Wyman, Cyril Crassin, and Nir Benty. 2022. The Falcor Rendering Framework. https://github.com/NVIDIAGameWorks/Falcor

Brian Karis. 2014. High-quality Temporal Supersampling. *Advances in Real-Time Rendering in Games, SIGGRAPH Courses* 1, 10.1145 (2014), 2614028–2615455.

Jaroslav Křivánek, Marcos Fajardo, Per H Christensen, Eric Tabellion, Michael Bunnell, David Larsson, and Anton Kaplanyan. 2010. Global Illumination across Industries. In *ACM SIGGRAPH Courses*. ACM Press.

Peter Kutz, Ralf Habel, Yining Karl Li, and Jan Novák. 2017. Spectral and Decomposition Tracking for Rendering Heterogeneous Volumes. *ACM Transactions on Graphics (Proceedings of SIGGRAPH)* 36, 4 (July 2017), 111:1–111:16. https://doi.org/10/gbxjxg

Mark Lee, Brian Green, Feng Xie, and Eric Tabellion. 2017. Vectorized Production Path Tracing. In *Proceedings of High Performance Graphics* (Los Angeles, California) *(HPG '17)*. Association for Computing Machinery, New York, NY, USA, Article 10, 11 pages. https://doi.org/10.1145/3105762.3105768

Edward Liu. 2022. DLSS 2.0 - Image Reconstruction for Real-Time Rendering with Deep learning. In *Game Developers Conference*.

Joel McCormack, Ronald Perry, Keith Farkas, and Norman Jouppi. 1999. Feline: Fast Elliptical Lines for Anisotropic Texture Mapping. In *Proceedings of SIGGRAPH*. 243–250. https://doi.org/10.1145/311535.311562

Microsoft. 2015. Direct3D 11.3 Functional Specification. https://microsoft.github.io/DirectX-Specs/d3d/archive/D3D11_3_FunctionalSpec.htm

Bailey Miller, Iliyan Georgiev, and Wojciech Jarosz. 2019. A Null-Scattering Path Integral Formulation of Light Transport. *ACM Transactions on Graphics (Proceedings of SIGGRAPH)* 38, 4 (July 2019), 44:1–44:13. https://doi.org/10/gf6rzb

Don P. Mitchell and Arun N. Netravali. 1988. Reconstruction Filters in Computer Graphics. *SIGGRAPH Comput. Graph.* 22, 4 (June 1988), 221–228. https://doi.org/10/fggxbg

Ken Museth. 2013. VDB: High-Resolution Sparse Volumes with Dynamic Topology. *ACM Transactions on Graphics* 32, 3 (July 2013), 27:1–27:22. https://doi.org/10/gfzq7s

Diego Nehab and Hugues Hoppe. 2011. Generalized sampling in computer graphics. *Microsoft Research, Redmond, WA, USA, Tech. Rep. MSR-TR-2011-16* (2011).

Jan Novák, Andrew Selle, and Wojciech Jarosz. 2014. Residual Ratio Tracking for Estimating Attenuation in Participating Media. *ACM Transactions on Graphics (Proceedings of SIGGRAPH Asia)* 33, 6 (Nov. 2014), 179:1–179:11. https://doi.org/10/f6r2nq

Shinji Ogaki. 2021. Vectorized Reservoir Sampling. In *SIGGRAPH Asia 2021 Technical Communications*. Association for Computing Machinery, Article 20, 4 pages. https://doi.org/10.1145/3478512.3488602

Marc Olano and Dan Baker. 2010. LEAN Mapping. In *Proceedings of the Symposium on Interactive 3D Graphics and Games*. 181–188. https://doi.org/10/fkbvpn

Art Owen and Yi Zhou. 2000. Safe and Effective Importance Sampling. *J. Amer. Statist. Assoc.* 95, 449 (2000), 135–143.

Matt Pharr, Wenzel Jakob, and Greg Humphreys. 2022. pbrt-v4. https://github.com/mmp/pbrt-v4

Matt Pharr, Wenzel Jakob, and Greg Humphreys. 2023. *Physically Based Rendering: From Theory to Implementation* (4th ed.). MIT Press, Cambridge, MA.

Thomas Porter and Tom Duff. 1984. Compositing Digital Images. *Computer Graphics (Proceedings of SIGGRAPH)* 18, 3 (July 1984), 253–259. https://doi.org/10/dzsnj2

William T. Reeves, David H. Salesin, and Robert L. Cook. 1987. Rendering Antialiased Shadows with Depth Maps. *Computer Graphics (Proceedings of SIGGRAPH)* (1987), 283–291. https://doi.org/10/bc4hw2

Sheldon M. Ross. 2019. *A First Course in Probability* (10th ed.). Pearson.

Peter Shirley. 1990. *Physically Based Lighting Calculations for Computer Graphics*. Ph. D. Dissertation. University of Illinois, Urbana–Champaign.

Peter Shirley, Changyaw Wang, and Kurt Zimmerman. 1996. Monte Carlo Techniques for Direct Lighting Calculations. *ACM Transactions on Graphics* 15, 1 (Jan. 1996), 1–36. https://doi.org/10/ddgbgg

Tomasz Stachowiak. 2015. Stochastic Screen-Space Reflections. In *Advances in Real-Time Rendering in Games, Part I (ACM SIGGRAPH Courses)*. https://doi.org/10/gf3s6n

Tim Sweeney and Paul Nettle. 2000. Texturing As In Unreal. https://www.flipcode.com/archives/Texturing_As_In_Unreal.shtml

Laszlo Szécsi, Laszlo Szirmay-Kalos, and Csaba Kelemen. 2003. Variance Reduction for Russian-roulette. *Journal of the World Society for Computer Graphics (WSCG)* 11, 1–3 (2003).

H. Takeda, S. Farsiu, and P. Milanfar. 2007. Kernel Regression for Image Processing and Reconstruction. *IEEE Transactions on Image Processing* 16, 2 (Feb. 2007), 349–366. https://doi.org/10/b4gfwp

Karthik Vaidyanathan, Marco Salvi, Bartlomiej Wronski, Tomas Akenine-Möller, Pontus Ebelin, and Aaron Lefohn. 2023. Random-Access Neural Compression of Material Textures. In *Proceedings of SIGGRAPH*.

Walt Disney Animation Studios. 2017. Cloud Data Set. https://disneyanimation.com/data-sets/

Lance Williams. 1983. Pyramidal Parametrics. *Computer Graphics (Proceedings of SIGGRAPH)* 17, 3 (July 1983), 1–11. https://doi.org/10/cq4xrd

Alan Wolfe, Nathan Morrical, Tomas Akenine-Möller, Ravi Ramamoorthi, A Ghosh, and LY Wei. 2022. Spatiotemporal Blue Noise Masks. In *Eurographics Symposium on Rendering*. 117–126.

Bartlomiej Wronski. 2021. Practical Gaussian filtering: Binomial filter and small sigma Gaussians. https://bartwronski.com/2021/10/31/practical-gaussian-filter-binomial-filter-and-small-sigma-gaussians/

Bartlomiej Wronski, Ignacio Garcia-Dorado, Manfred Ernst, Damien Kelly, Michael Krainin, Chia-Kai Liang, Marc Levoy, and Peyman Milanfar. 2019. Handheld Multi-Frame Super-Resolution. *ACM Transactions on Graphics (Proceedings of SIGGRAPH)* 38, 4 (July 2019), 28:1–28:18. https://doi.org/10/gf6d4v

Chris Wyman and Morgan McGuire. 2017. Hashed alpha testing. In *Proceedings of the 21st ACM SIGGRAPH Symposium on Interactive 3D Graphics and Games*. 7:1–7:9.

Lei Yang, Shiqiu Liu, and Marco Salvi. 2020. A Survey of Temporal Antialiasing Techniques. *Computer Graphics Forum* 39, 2 (2020), 607–621.

Jihun Yu and Greg Turk. 2013. Reconstructing surfaces of particle-based fluids using anisotropic kernels. *ACM Transactions on Graphics (TOG)* 32, 1 (2013), 1–12.

Supplemental Material for "Filtering After Shading With Stochastic Texture Filtering"

S.1 LINEAR FILTERS

Direct application of the array sampling algorithm from Section 2.2 and then Equation 5 gives the following estimator for linear interpolation over $[0, 1]$, $\mathit{lerp}(v_0, v_1, t) = (1 - t)v_0 + tv_1$:

$$\langle \mathit{lerp} \rangle = \begin{cases} v_0, & \text{if } \xi > t \\ v_1 & \text{otherwise.} \end{cases} \tag{15}$$

Bilinear interpolation of values at the four corners of the unit square, $\mathit{bilerp}\,(v_{00}, v_{10}, v_{01}, v_{11}, s, t)$, can be implemented with nested linear interpolations. Applying the same approach and reusing the sample, we have:

$$\langle \mathit{bilerp} \rangle(s,t) = \begin{cases} v_{00}, & \text{if } \xi > s \text{ and } (\xi - s)/(1 - s) > t \\ v_{01}, & \text{if } \xi > s \text{ and } (\xi - s)/(1 - s) \le t \\ v_{10}, & \text{if } \xi \le s \text{ and } \xi/s > t \\ v_{11}, & \text{otherwise.} \end{cases} \tag{16}$$

It is straightforward to extend this estimator to trilinear interpolation, as used with MIP mapping and 3D voxel grids. More generally, the technique can be applied to n-dimensional interpolation, reducing from 2^n texture lookups to a single one.

S.2 FILTER KERNELS

For reference, we summarize some commonly used filter kernels, starting with interpolating polynomials. Their one-dimensional definitions are listed here; n-dimensional filtering is performed by filtering each dimension independently—the filters are separable. See Figure 16 for graphs of the kernels and how they filter an example set of samples.

The 0th-order kernel is a unit box function, which corresponds to nearest-neighbor sampling.

$$K_0(t) = \begin{cases} 1, & \text{if } |t| < \frac{1}{2} \\ 0 & \text{otherwise.} \end{cases} \tag{17}$$

The first order kernel is the unit tent, which gives linear sampling.

$$K_1(t) = \begin{cases} (1 - |t|), & |t| < 1 \\ 0 & \text{otherwise.} \end{cases} \tag{18}$$

The cubic polynomial kernel is defined as

$$K_3(t) = \begin{cases} (a+2)|t|^3 - (a+3)|t|^2 + 1, & |t| < 1 \\ a|t|^3 - 5a|t|^2 + 8a|t| - 4a, & 1 < |t| < 2 \\ 0 & \text{otherwise,} \end{cases} \tag{19}$$

where a is an extra degree of freedom in cubic interpolation. Mitchell and Netravali [Mitchell and Netravali 1988] recommend a value of −0.5 and it is the closest to Lanczos2, a windowed sinc kernel [Duchon 1979] while keeping low evaluation cost.

The Lanczos n kernel has a spatial support of $2n$ and is defined:

$$K_{Ln}(t) = \begin{cases} 1 & t = 0, \\ \frac{\sin(x\pi)}{x} \frac{\sin(\pi x/n)}{x/n}, & 0 < |t| < n \\ 0 & \text{otherwise.} \end{cases} \tag{20}$$

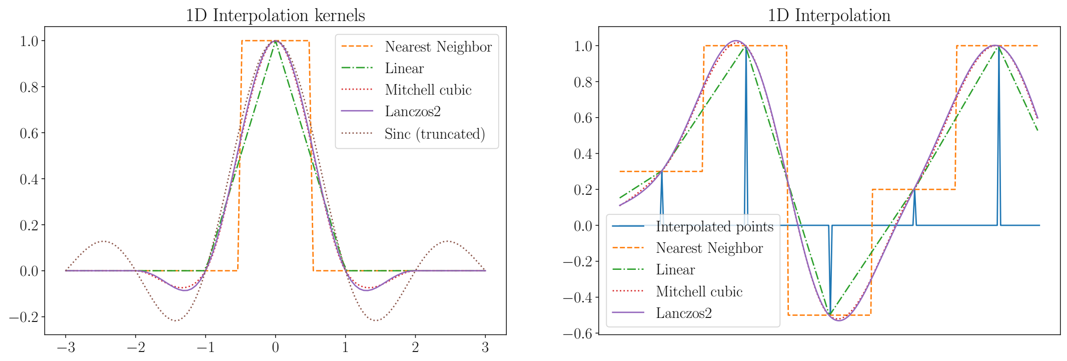

Fig. 16. Commonly used 1D interpolation kernels and resulting interpolation of a random 1D points – nearest-neighbor (box filter), linear, Mitchell cubic, and Lanczos2. Lanczos2 is almost identical to the Mitchell kernel.

S.2.1 Convolutional

The non-interpolating cubic B-spline is often used as it approximates the Gaussian filter and produces smooth results while being cheap to evaluate. It is used for the offline rendering example in Figure 1.

$$K_{bs}(t) = \frac{1}{6}\begin{cases} 4 - 3t^2(2 - |t|) & |t| \le 1 \\ (2 - |t|)^3 & 1 < |t| \le 2 \\ 0 & \text{otherwise.} \end{cases} \tag{21}$$

S.3 SPECTRAL EFFECTS OF NONLINEARITIES

Without loss of generality, let's consider a 1D signal. We start by looking at the simplest analytical nonlinearities, polynomials. Applying a squaring function to a signal comprising a single sinusoid function $sin(w)$ doubles the frequency from a well-known trigonometric identity:

$$\sin^2(wx) = \frac{1 - \cos(2wx)}{2} \tag{22}$$

Considering two sine functions, we get:

$$(\sin(w_0x) + \sin(w_1x))^2 = \frac{-2\cos((w_0 + w_1)x) - \cos(2w_1x) + 2\cos((w_0 - w_1)x) - \cos(2w_0x) + 2}{2} \tag{23}$$

We observe so-called *intermodulations* and the appearance of new frequencies depending on both input signal frequencies. The maximum new frequency is the maximum of $2w_0$ and $2w_1$.

The same pattern continues for sums of multiple trigonometric functions. Similarly, the power N and a degree N polynomial produce up to the N-multiple of the highest frequency present in the original signal.

Real nonlinear and practical functions are not just polynomials, but a similar analysis can be performed. We observe a similar effect of new harmonics appearing, including inter-modulations of the more complex signals. One of the easiest ways to understand an approximate effect of an arbitrary non-linearity is by considering the Taylor series expansion of the original function around the sample points. The smoother the non-linear function and better approximated by a lower order polynomial around all the values present in the original signal, the less high frequencies are produced. Very highly discontinuous functions and ones with high local curvatures produce a lot

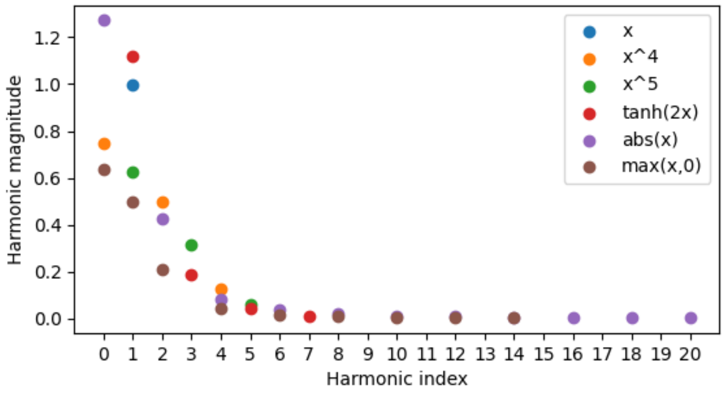

Fig. 17. Effect of various nonlinearities applied to a single sine function creating new harmonics and higher signal frequencies.

of new harmonics and very high-frequency content. We plot the frequency effect of some common nonlinearities on a single sine function in Figure 17.

Any non-trivial nonlinearity will introduce a significant amount of new, higher-frequency signal content. Functions that are only $C0$ continuous, such as maximum (clipping) or absolute values dramatically increase the signal bandwidth.

S.3.1 Nonlinearity introduced aliasing

One of the consequences of nonlinearities adding new frequency content is that they can introduce significant aliasing on both continuous data to be sampled (by changing its bandwidth and increasing the required sampling frequency if no additional lowpass filtering is applied) and already sampled, discrete data.

Consider what happens to a simple sine function that gets sampled at different frequencies:

$$\begin{aligned}\sin([-1, -\tfrac{\sqrt{2}}{2}, 0, \tfrac{\sqrt{2}}{2}, 1, \tfrac{\sqrt{2}}{2}])^2 &= [1, \tfrac{1}{2}, 0, \tfrac{1}{2}, 1, \tfrac{1}{2}] \\ \sin([-1, 0, 1, 0, -1, 0])^2 &= [1, 0, 1, 0, 1, 0] \\ \sin([-1, 1, -1, 1, -1, 1])^2 &= [1, 1, 1, 1, 1, 1]\end{aligned} \tag{24}$$

In the second and third examples, we observe aliasing and incorrect frequencies appearing despite critical sampling of the original function. When the original sine is sampled at a higher signal frequency, we can recover the second harmonic and the constant bias correctly. To prevent aliasing when applying a nonlinearity, the processed signal has to be either sampled at a significantly higher frequency than as implied by the Nyquist theorem or upsampled to a higher frequency before applying the nonlinearity.

This is not an intuitively expected, but a common problem in rendering and computer graphics. The resulting aliasing can be severe since rendering always operates on discrete signals and introduces strong nonlinearities. In many ways, the growing popularity of post-filtering techniques has hidden some of the most severe instances of this problem but can manifest itself even there. When applying anti-aliasing on the non-tone-mapped scene image, the tone-mapping operator can reintroduce significant aliasing, irrespective of the anti-aliasing technique used (MSAA, temporal AA). This leads to complex practices, such as multiple anti-aliasing stages in the modern rendering pipeline (for post-processing buffers, final color buffers, reflection buffers, and more). Aliasing from nonlinearity affects the stochastic texture filtering as well, both minification and magnification.

When the shading happens in lower resolution (during stochastic magnification), aliasing is increased. The converse effect is present during the stochastic minification – aliasing is significantly reduced as shading occurs at a higher resolution.

S.4 FILTER IMPLEMENTATIONS

For reference, implementations of most of the stochastic filters in the paper are in the following. (We skip cases like the stochastic trilinear filter, since it is a straightforward modification to the stochastic bilinear filter, for example.)

All of the following parameters take a parameter `u`, which should be a uniform random sample in $[0, 1]$ and a lookup point that is assumed to be with respect to texture raster coordinates (i.e., it ranges between 0 and the texture's resolution in each dimension). They return (by reference) a remapped uniform random sample that may be reused and stochastically-sampled integer texel coordinates.

`StochasticBilinear` stochastically samples the bilinear function.

Listing 1. Sampling a 2D bilinear kernel

```
Point2i StochasticBilinear(Point2f st, float &u) {
    int s = std::floor(st[0]), t = std::floor(st[1]);
    float ds = st[0] - std::floor(st[0]);
    float dt = st[1] - std::floor(st[1]);
    if (u < ds) {
        ++s;
        u /= ds;
    } else
        u = (u - ds) / (1 - ds);

    if (u < dt) {
        ++t;
        u /= dt;
    } else
        u = (u - dt) / (1 - dt);

    return Point2i(s, t);
}
```

The bicubic kernel based on Equation 21 is stochastically sampled by `StochasticBicubic`. The computed weights correspond to the weights for the two texels to the left of the lookup point (`weights[0]` and `weights[1]`) and the two to the right (`weights[2]` and `weights[3]`). This implementation stores each dimension's filter weights in an array and then samples a single filter tap.

Listing 2. Sampling a B-spline cubic kernel in 2D

```
Point2i StochasticBicubic(Point2f st, float &u) {
    // Compute filter weights
    auto weights = [](float t, float w[4]) {
        float t2 = t*t;
        w[0] = (1.f/6.f) * (-t*t2 + 3*t2 - 3*t + 1);
        w[1] = (1.f/6.f) * (3*t*t2 - 6*t2 + 4);
        w[2] = (1.f/6.f) * (-3*t*t2 + 3*t2 + 3*t + 1);
        w[3] = (1.f/6.f) * t*t2;
    };
    float ws[4], wt[4];
    weights(st[0] - std::floor(st[0]), ws);
    weights(st[1] - std::floor(st[1]), wt);

    // Sample index based on weights in each dimension.
    int s0 = std::floor(st[0]-1), t0 = std::floor(st[1]-1);
    int s = SampleDiscrete(ws, u, nullptr, &u);
    int t = SampleDiscrete(wt, u, nullptr, nullptr);
    return {s0+s, t0+t};
}
```

In the following implementation, `StochasticTricubic` uses weighted reservoir sampling to sample the filter in each dimension. In this way, the filter weights can be computed on the fly and do not all need to be stored at once.

Listing 3. Sampling a cubic B-spline kernel in 3D

```
Point3i StochasticTricubic(Point3f pIndex, float &u) {
    int ix = std::floor(pIndex.x);
    int iy = std::floor(pIndex.y);
    int iz = std::floor(pIndex.z);
    float deltas[3] = {pIndex.x - ix, pIndex.y - iy, pIndex.z - iz};

    int idx[3];
    for (int i = 0; i < 3; ++i) {
        float sumWt = 0;
        float t = deltas[i];
        float t2 = t*t;

        // Weighted reservoir sampling, first tap always accepted
        float w0 = (1.f/6.f) * (-t*t2 + 3*t2 - 3*t + 1);
        sumWt = w0;
        idx[i] = 0;

        // Weighted reservoir sampling helper
        auto wrs = [&](int j, float w) {
            sumWt += w;
            float p = w/sumWt;
            if (u < p) {
                idx[i] = j;
                u /= p;
            } else
                u = (u - p) / (1 - p);
        };
        // Sample the other 3 filter taps
        wrs(1, (1.f/6.f) * (3*t*t2 - 6*t2 + 4));
        wrs(2, (1.f/6.f) * (-3*t*t2 + 3*t2 + 3*t + 1));
        wrs(3, (1.f/6.f) * t*t2);
    };

    // idx stores the index of the sampled filter tap in
    // each dimension.
    return Point3i(ix-1+idx[0], iy-1+idx[1], iz-1+idx[2]);
}
```

Our implementation for sampling the EWA kernel [Greene and Heckbert 1986; Heckbert 1989] is in `StochasticEWA`. It largely follows the implementation of EWA filtering in *pbrt*, except that as filter weights are computed in the innermost loop, vectorized weighted reservoir sampling [Ogaki 2021] is used to select a single filter tap.

Listing 4. Stochastic sampling of the EWA kernel

```
Point2i StochasticEWA(Point2f st, Vector2f dst0, Vector2f dst1,
                      float &u) {
    // Find ellipse coefficients that bound EWA filter region
    float A = Sqr(dst0[1]) + Sqr(dst1[1]) + 1;
    float B = -2 * (dst0[0] * dst0[1] + dst1[0] * dst1[1]);
    float C = Sqr(dst0[0]) + Sqr(dst1[0]) + 1;
    float invF = 1 / (A * C - Sqr(B) * 0.25f);
    A *= invF;
    B *= invF;
    C *= invF;

    // Compute the ellipse's $(s,t)$ bounding box in texture space
    float det = -Sqr(B) + 4 * A * C;
    float invDet = 1 / det;
    float uSqrt = SafeSqrt(det * C), vSqrt = SafeSqrt(A * det);
    int s0 = std::ceil(st[0] - 2 * invDet * uSqrt);
    int s1 = std::floor(st[0] + 2 * invDet * uSqrt);
    int t0 = std::ceil(st[1] - 2 * invDet * vSqrt);
    int t1 = std::floor(st[1] + 2 * invDet * vSqrt);

    // Scan over ellipse bound and evaluate quadratic equation
    float sumWts = 0;
    Point2i coords;
    for (int it = t0; it <= t1; ++it) {
        float tt = it - st[1];
        for (int is = s0; is <= s1; ++is) {
            float ss = is - st[0];
            float r2 = A * Sqr(ss) + B * ss * tt + C * Sqr(tt);
            if (r2 >= 1)
                continue;

            int index = std::min<int>(r2 * MIPFilterLUTSize,
                                      MIPFilterLUTSize - 1);
            float weight = MIPFilterLUT[index];
            if (weight <= 0)
                continue;

            sumWts += weight;
            float p = weight / sumWts;
            if (u < p) {
                coords = Point2i(is, it);
                u /= p;
            } else
                u = (u - p) / (1 - p);
        }
    }
    return coords;
}
```

S.4.1 The interpolating (negative lobe) bicubic filter

In Section 5 we presented results of real-time rendering with a stochastically estimated variant of the Mitchell bicubic filter. This filter has negative lobes and for most of the fractional subpixel offsets, has a mix of negative and positive weights. As described in Section 2.2, the solution that minimizes the variance of such a filter splits the integral into two parts.

From the set of all filter weights, we consider the sets of positive and negative weights separately and select a sample from each of the sets independently. Then, the filter takes two samples, weighted by the sum of the absolute values of each of the sampling sets. One way of implementing it uses weighted reservoir sampling with warping (also described in Section 2.2) and two separate reservoirs for the negative and positive samples. An example implementation in C++-like pseudocode is presented in Listing 5.

Listing 5. Sampling an interpolating (negative lobe) bicubic kernel.

```
TexelValue SampleBicubic(const Texture& texture,
                         const Vector2& pixel_coord,
                         float& u) {
    const Vector2 top_left = floor(pixel_coord);
    const Vector2 fract_offset = pixel_coord - top_left;

    float pos_weights_sum = 0.0f;
    float neg_weights_sum = 0.0f;
    Vector2 selected_neg_offset;
    Vector2 selected_pos_offset;
    for (int dy = -1; dy <= 2; ++dy) {
        float weight_dy = MitchellCubic(fract_offset.y - dy);
        for (int dx = -1; dx <= 2; ++dx) {
            float weight_dx = MitchellCubic(fract_offset.x - dx);
            float w = weight_dy * weight_dx;
            float& selected_reservoir_sum = w < 0.0f ?
                                            neg_weights_sum :
                                            pos_weights_sum;
            Vector2& selected_reservoir = w < 0.0f ?
                                            selected_neg_offset :
                                            selected_pos_offset;

            selected_reservoir_sum += abs(w);
            float p = abs(w) / selected_reservoir_sum;
            if (u <= p) {
                selected_reservoir = Vector2(dx, dy);
                u = u / p;
            } else {
                u = (u - p)/(1 - p);
            }
        }
    }
    Vector2 pos_coord = top_left + selected_pos_offset;
    TexelValue sampled_val = pos_weights_sum *
                             SampleTexture(texture, pos_coord);
    // It's possible to not have any negative sample, for example,
    // when the fractional offset is exactly 0 or very small.
    if (neg_weights_sum != 0.0f) {
        Vector2 neg_coord = top_left + selected_neg_offset;
        sampled_val += -neg_weights_sum *
                       SampleTexture(texture, neg_coord);
    }
    return sampled_val;
}
```

S.4.2 Real-time discrete and filter importance sampling

In Section 5 we compared discrete sampling to FIS and their pros and cons for filtering with an infinite Gaussian, discrete approximation, and the impact on the image quality. In Listing 6 and Listing 7 we present an HLSL implementation of both filters. Both implementations produce perturbed UVs for use with a texture sampler set to the Nearest Neighbor texture filtering mode, or to be used with integer Load instructions. Filter Importance Sampling is significantly simpler and uses less arithmetic, but this implementation requires the use of two random variables.

Listing 6. Gaussian Filter Importance Sampling.

```
float2 boxMullerTransform(float2 u)
{
    float2 r;
    float mag = sqrt(-2.0 * log(u.x));
    return mag * float2(cos(2.0 * PI * u.y), sin(2.0 * PI * u.y));
}

float2 FISGaussianUV(float2 uv, float2 dims,
                                      float sigma, float2 u)
{
    float2 offset = sigma * boxMullerTransform(u);

    return uv + offset / dims;
}
```

Listing 7. Gaussian Filter Discrete Sampling.

```
float2 discreteStochasticGaussianUV(float2 uv, float2 dims,
                                    float sigma, float u)
{
    float2 uv_full = uv * dims - 0.5;
    float2 left_top = floor(uv_full);
    float2 fract_part = uv_full - left_top;

    float inv_sigma_sq = 1.0f / (sigma*sigma);

    float weights_sum = 0.0f;
    float2 offset = float2(0.0f, 0.0f);

    #define FILTER_EXTENT 4
    #define FILTER_NEG_RANGE ((EXTENT-1)/2)
    #define FILTER_POS_RANGE (EXTENT-NEG_RANGE)
    for (int dy = -NEG_RANGE; dy < POS_RANGE; ++dy) {
        for (int dx = -NEG_RANGE; dx < POS_RANGE; ++dx) {
            float offset_sq = dot(float2(dx, dy) - fract_part,
                                  float2(dx, dy) - fract_part);
            float w = exp(-0.5 * dist_sq * inv_sigma_sq);
            weights_sum += w;
            float p = w / weights_sum;
            if (u <= p) {
                offset = float2(dx, dy);
                u = u / p;
            } else {
                u = (u - p)/(1 - p);
            }
        }
    }

    return (left_top + offset + 0.5) / dims;
}
```

S.4.3 Real-time anisotropic filtering

In Section 5 we described the stochastic anisotropic LOD for use with screen-space jittering. In Listing 8 we include the HLSL code for this computation.

Listing 8. Texture MIP computation used in real-time implementation.

```
float computeLodAniso(float2 dims, float2 textureGradX, float2 textureGradY,
                      float minLod, float maxLod, float u)
{
    float dudx = dims.x * textureGradX.x;
    float dvdx = dims.y * textureGradX.y;
    float dudy = dims.x * textureGradY.x;
    float dvdy = dims.y * textureGradY.y;

    // Find min and max ellipse axis
    maxAxis = float2(dudy, dvdy);
    float2 minAxis = float2(dudx, dvdx);
    if (dot(minAxis, minAxis) > dot(maxAxis, maxAxis))
    {
        minAxis = float2(dudy, dvdy);
        maxAxis = float2(dudx, dvdx);
    }

    float minAxisLength = length(minAxis);
    float maxAxisLength = length(maxAxis);

    float maxAnisotropy = 64;

    if ( minAxisLength > 0 &&
        (minAxisLength * maxAnisotropy) < maxAxisLength)
    {
        float scale = maxAxisLength / (minAxisLength * maxAnisotropy);
        minAxisLength *= scale;
    }
    return clamp(log2(minAxisLength) + (u - 0.5), minLod, maxLod);
}
```